

# In vivo fundus imaging and computational refocusing with a diffuser-based fundus camera

COREY SIMMERER,<sup>1</sup> MARISA MORAKIS,<sup>1</sup> LEI TIAN,<sup>2</sup> LIA GOMEZ-PEREZ,<sup>1,3,4</sup> T.Y. ALVIN LIU,<sup>5</sup> AND NICHOLAS J. DURR<sup>1,5,\*</sup>

<sup>1</sup>*Department of Biomedical Engineering, Johns Hopkins University, Baltimore, MD, USA*

<sup>2</sup>*Department of Electrical and Computer Engineering, Boston University, Boston, MA, USA*

<sup>3</sup>*Wellman Center for Photomedicine, Massachusetts General Hospital, Harvard Medical School, Boston, MA, USA*

<sup>4</sup>*Harvard-MIT Health Sciences and Technology, Massachusetts Institute of Technology, Cambridge, MA, USA*

<sup>5</sup>*Wilmer Eye Institute, Johns Hopkins University School of Medicine, Baltimore, MD, USA*

\*[ndurr@jhu.edu](mailto:ndurr@jhu.edu)

**Abstract:** Access to eye care can be expanded with high-throughput, easy-to-use, and portable diagnostic tools. Phase-mask encoded imaging could improve these aspects of the fundus camera by enabling computational refocusing without any moving parts. This approach circumvents the need to adjust lenses to compensate for accommodation or refractive errors. We developed a computational fundus camera by introducing a holographic diffuser at the conjugate plane to the ocular pupil, resulting in a laterally shift-invariant point-spread function. We demonstrate computational refocusing of a model eye fundus over a large range of defocus errors (up to  $\pm 12D$ ). We also show computationally-refocused color in vivo human fundus images with a  $\geq 35$ -degree field-of-view (FOV). This technology could eventually be combined with the wavefront-sensing capabilities of phase-mask encoded imaging to create a compact ophthalmic imaging system that simultaneously captures a fundus image and performs aberrometry.

## 1. Introduction

The comprehensive eye examination is the foundational procedure to assess and begin addressing eye disease. There are several components to this procedure to examine nearly every part of the eye [1]. Fundus examination is a key component: diseases of the fundus such as diabetic retinopathy, glaucoma, and age-related macular degeneration are leading causes of visual impairment and blindness globally [2]. Yet, even in high-risk populations in high-resource countries, many people do not receive regular fundus examinations, resulting in unmanaged vision loss and blindness [3,4]. In low-resource populations, the situation is compounded by the lack of trained ophthalmologists [5]. There is thus an unmet need to increase the accessibility of critical fundus examinations.

A useful tool for early detection of retinopathies and glaucoma is the digital fundus camera [6]. Fundus cameras simultaneously flood-illuminate the back of the eye and image it through the pupil. Non-mydratic (no pupil dilation) fundus cameras are typically aligned by a technician to a patient's eye using near-infrared (NIR) illumination to avoid pupil constriction. Aligning to a precise axial and lateral position at the correct angle is necessary to capture a fundus photo in the proper field of view (FOV) without bright reflections [7]. During the alignment process, the camera's optics must also be adjusted to compensate for the defocus from refractive errors and accommodation. Once the alignment and focus are satisfactory, the clinical technician takes a white light flash photograph to be taken with an exposure time shorter than the pupil light response of approximately 200 ms for visible light [8]. Capturing a high-quality fundus image requires significant skill and precision, necessitating operation by a trained clinical technician [9].

Significant barriers to accessing these exams include the high cost of equipment, the high skill level required to perform precise and sensitive measurements, and the shortage of trained

clinicians and technicians in remote areas [5, 9, 10]. Developing new imaging tools to simplify eye disease diagnosis and increase clinical throughput could help reduce these screening barriers. Recently developed portable fundus cameras aim to alleviate some barriers to access [11]. However, these handheld devices generally have a limited FOV and are challenging to align and focus. Accordingly, they have yet to garner much clinical adoption [9, 11, 12]. Meanwhile, deep-learning based screening for retinopathies has the potential to greatly increase the reach of fundus examination [13]. However, AI-based screening methods still require quality images of the fundus as input, which are still difficult to acquire. Results from Shou et al. showed non-diagnostic quality images in more than half of nondilated AI-screened patients [14]. Creating a device that simplifies fundus image capture has great potential to reduce costs, increase throughput, and deskill the comprehensive eye examination.

### *1.1. Computational lensless imaging*

The emerging field of computational lensless imaging promises new capabilities for imaging with a standard image sensor, such as single-shot 3D imaging [15, 16], computational refocusing [17], and lightfield imaging [18]. One method of computational imaging uses an encoding mask instead of a lens to multiplex plenoptic information onto the image sensor [19]. Prior knowledge of the optical properties of the mask then enables computational reconstruction of the captured lightfield.

One such encoding mask is a holographic diffuser, as demonstrated by Antipa et al. [17]. A diffuser produces a sharp caustic pattern as a point spread function (PSF) that is relatively shift-invariant for lateral movements of a point and is magnified or demagnified for axial movements of a point. Prior characterization of the PSF enables image reconstruction from diffuser measurements. The axial dependence of the PSF enables 3D imaging and computational refocusing. This feature is particularly desirable in a fundus camera, as it would allow the focusing process to take place after image capture.

### *1.2. Related works*

Li et al. first proposed the diffuser-based computational imaging funduscope [20]. They used a 4- $f$ , infinite-conjugate system, relaying the wavefront emerging from a model eye to a diffuser placed in front of the image sensor. Flood illumination of the fundus was accomplished using a beamsplitter to coaxially illuminate and image through the pupil. Crossed polarizers were used to prevent the strong model corneal reflections from passing to the image sensor. They tested the grayscale imaging and computational refocusing capabilities with varying levels of defocus error.

Adapting a color computational fundus camera for in vivo use presents additional challenges. The crossed-polarizer method of illumination effectively eliminates corneal reflections but also attenuates much of the fundus signal. This is highly undesirable in vivo because there are irradiation limits for fundus illumination and the quality of reconstruction is highly dependent on SNR and the image sensor's dynamic range. Conventional clinical fundus cameras use an alternative optical design in a non 4- $f$  configuration with a holed mirror to eliminate the need for polarizers while keeping illumination and imaging pathways coaxial. We utilize this optical design in our computational fundus camera, enabling high SNR and short exposure time for in vivo imaging.

This paper details our in vivo color computational fundus photography methods using a diffuser-based phase mask. We evaluate the optical performance measures of the imaging system. Finally, we demonstrate the first diffuser-based in vivo fundus images and demonstrate computational refocusing.

## 2. Methods

### 2.1. Overview

At a high level, our computational imaging system is constructed by modifying a commercial non-mydratric fundus camera with a diffuser-based camera similar to Antipa et al. [15]. An overview of the computational imaging workflow and system layout is shown in Fig. 1. Akin to the layout presented by Li et al. [20], a holographic diffuser is placed conjugate to the pupil. An image sensor is positioned at an axial distance that optimizes the sharpness of the PSF. The PSF is approximately linear and shift-invariant (LSI) in the transverse axis, meaning that the sensor measurement can be represented by a simple convolution of the object at a specific axial plane with the PSF corresponding to that plane. The PSF depends on the axial distance of the object behind the lens and scales with this defocus error [15]. These PSFs are measured a single time to calibrate the system. For color fundus imaging, three consecutive diffuser images are collected in red, green, and blue illumination on a monochromatic sensor. The resulting image is deconvolved with the PSF calibration stack using a regularized inverse filter, and the most focused image is selected from the resulting focal stack.

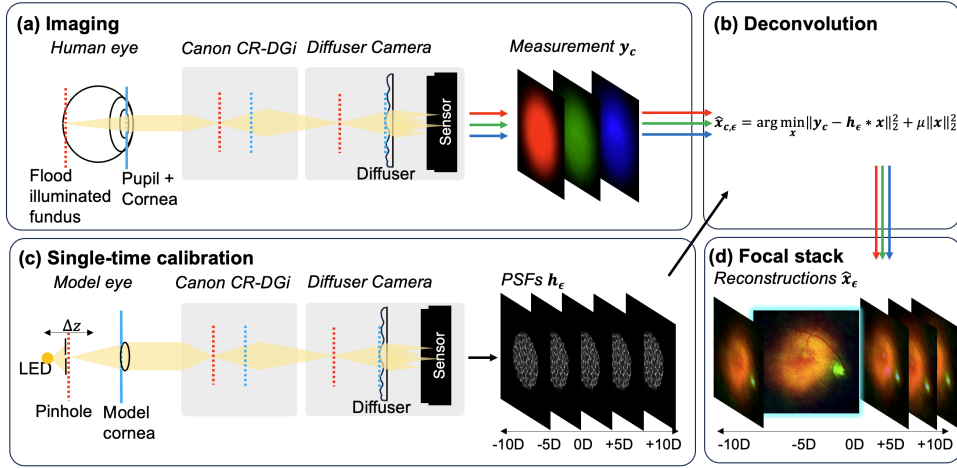


Fig. 1. Overview of the computational fundus camera. (a) Measurements of the fundus are captured by connecting a relay lens, diffuser, and image sensor to the imaging port of a commercial fundus camera. Three consecutive measurements,  $y_c$ , using red, green, and blue light illumination are taken with the diffuser in a conjugate plane to the pupil. (b) The three color channels are independently deconvolved with each PSF in the calibration stack. (c) The system is calibrated by directly measuring the PSF over a range of axial displacements from the focal plane of the model cornea, inducing a range of defocus errors,  $\epsilon$ . (d) An image is reconstructed from each color channel for each PSF and the sharpest image is selected from this stack.

### 2.2. Optical hardware

We used an existing commercial fundus camera (CR-DGi, Canon) as the platform for our novel computational fundus camera. This design was chosen because existing non-mydratric fundus cameras are housed on a translating base that eases alignment with the human eye. Additionally, the illumination and imaging pathways of the commercial system are optimized for non-mydratric use. The Canon CR-DGi also has a flip mirror to switch between the infrared alignment camera and the imaging camera. We removed the infrared alignment camera and replaced it with the

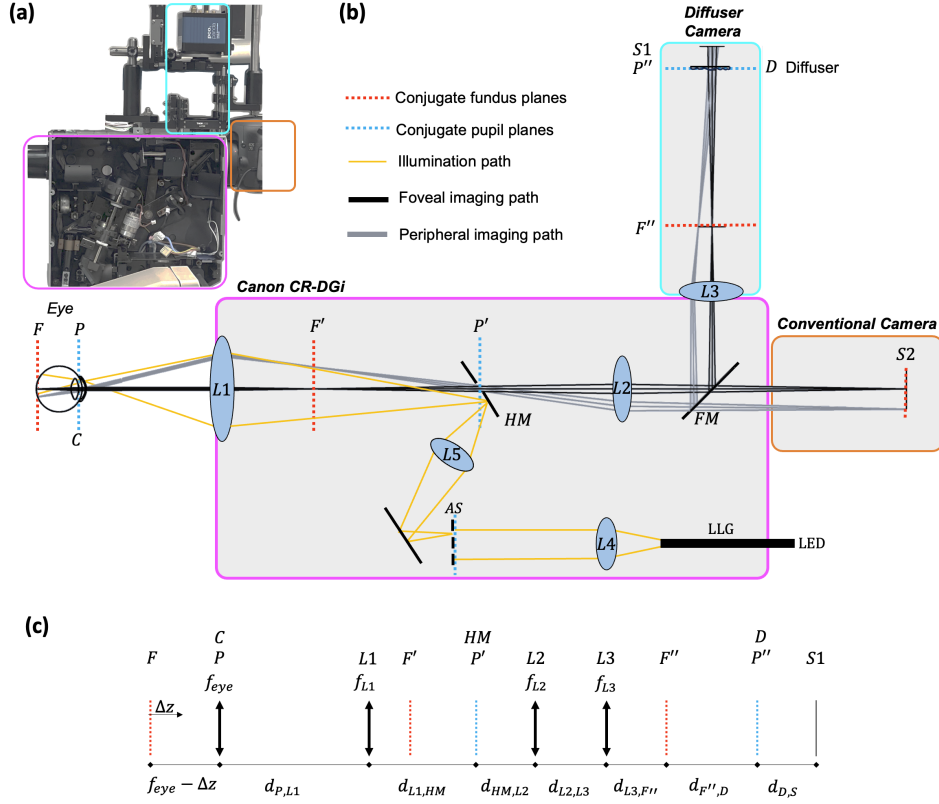


Fig. 2. Optical layout of the computational fundus camera. (a) Photo of the system with the main subsystems highlighted. (b) Annotated Zemax model of the system using paraxial lenses. Flood illumination of the fundus is provided with LEDs through a liquid light guide (LLG). The annular slit (AS) is imaged to the outer edges of the pupil of the eye. Remitted light from the fundus is collected from the center of the pupil that is conjugate with a holed mirror (HM). A conventional image of the fundus is formed on the sensor, S2. For diffuser-based imaging, the flip mirror (FM) directs the light upward through L3, which forms a conjugate pupil plane at the diffuser. The diffuser measurement is taken with S1 at a distance  $d_{D,S1}$  behind the diffuser. Note that the illumination pathway diagram has been shortened for illustrative purposes. (c) Reduced model of the diffuser imaging pathway with conjugate planes and distance variables defined. Values for these parameters are in Tables 1 and 2. Defocus error may be applied to the reduced eye by adjusting the distance between  $F$  and  $P$  by  $\Delta z$ .

diffuser-based computational camera ("diffuser camera" in Fig. 2) while keeping the conventional imaging camera (EOS 7D, Canon) in place. This allows easy switching between conventional and diffuser imaging.

The illumination pathway of the system is nearly identical to the original commercial fundus camera with the internal lenses in the housing unchanged (L1, L4, L5 in Fig. 2). Careful optical design is necessary to simultaneously illuminate and image the fundus. The illumination and imaging paths must be coaxial and pass through the cornea and pupil, which is much more reflective than the fundus [21, 22]. The original flash lamp was replaced with a liquid light guide (LLG03-4H, Thorlabs) connected to an LED light source (Lumen 1600-LED, Prior Scientific) with multiple selectable wavelengths in the visible and NIR range. The illumination is collimated

with L4 (Figure 2) and is passed through an annular slit (AS). The image of the ring is imaged onto the holed mirror (HM) with L5 and then imaged onto the pupil with the objective lens L1. The illumination ring is centered on the periphery of the pupil and results in flood illumination of the fundus while leaving the inner aperture available for back-reflection-free imaging.

The light remitted from the retina propagates back through the pupil and cornea, is relayed through the aperture in HM with L1 and L2, and is either imaged to a conventional camera or directed to the diffuser system via a flip mirror FM. For conventional fundus imaging, L2 is adjusted with axial movements to accommodate for defocus error (myopia or hyperopia), whereas for diffuser imaging, L2 is fixed. For the diffuser imaging path, the flip mirror reflects the light through L3 (AC254-100-A,  $f=100$  mm, Thorlabs) to create a conjugate pupil plane at a  $0.5^\circ$  holographic diffuser (#47-988, Edmund Optics). An image sensor (pco.panda 4.2 bi UV, Excelitas Technologies) is placed 11 mm behind the diffuser, which was found to be the location that produces the sharpest caustic PSF. We modeled this path in Zemax using paraxial lenses to produce the ray diagram in Fig. 2. A full list of optical parameters of the components is in Table 1 in the appendix.

### 2.3. Reconstruction

To computationally reconstruct the image from the diffuser measurement, we first model the object (the fundus) as a surface in 3D space at some axial depth behind the cornea associated with some defocus error,  $\epsilon$ . We assume the fundus is approximately flat. Consistent with linear and shift-invariant (in other reports and our PSF measurements, our system is approximately LSI in each transverse plane [15, 20]. The PSF for a given plane with an associated defocus error is  $\mathbf{h}_\epsilon$ . Because the system is LSI, we model the measurement,  $\mathbf{y}$ , of a fundus,  $\mathbf{x}$ , with convolution:

$$\mathbf{y} = \mathbf{h}_\epsilon * \mathbf{x} \quad (1)$$

We also assume that the illumination field is flat and that the PSF does not vary significantly with wavelength. The wavelength of illumination and sensor noise can be added to the forward model. The object at a given color of illumination is represented by  $\mathbf{x}_c$ , and the resulting measurement by  $\mathbf{y}_c$ . The noise model is additive white Gaussian noise,  $\mathbf{n}$ .

$$\mathbf{y}_c = \mathbf{h}_\epsilon * \mathbf{x}_c + \mathbf{n} \quad (2)$$

The reconstruction task is to estimate the underlying fundus,  $\mathbf{x}_c$ , given the measurement  $\mathbf{y}_c$ . We estimate the fundus image for each color at each defocus error,  $\hat{\mathbf{x}}_{\epsilon,c}$ , using Tikhonov regularization.

$$\hat{\mathbf{x}}_{\epsilon,c} = \arg \min_{\mathbf{x}} \|\mathbf{y}_c - \mathbf{h}_\epsilon * \mathbf{x}\|_2^2 + \mu \|\mathbf{x}\|_2^2 \quad (3)$$

Regularization strength is controlled by  $\mu$ , which is adjustable and chosen empirically. The first term minimizes  $L_2$ -norm of the difference between the model and the measurement. The second term regularizes the output by penalizing the  $L_2$ -norm of the estimate. This convex optimization problem can be solved efficiently in the Fourier domain [23].  $\hat{\mathbf{X}}_{\epsilon,c}$  is the Fourier transform of the estimated signal,  $\hat{\mathbf{x}}_{\epsilon,c}$ .  $\mathbf{H}_\epsilon$  and  $\mathbf{Y}_c$  are the Fourier transforms of  $\mathbf{h}_\epsilon$  and  $\mathbf{y}_c$ , respectively.

$$\hat{\mathbf{x}}_{\epsilon,c} = \mathcal{F}^{-1} \{ \hat{\mathbf{X}}_{\epsilon,c} \} = \mathcal{F}^{-1} \left\{ \frac{\mathbf{H}_\epsilon^*}{|\mathbf{H}_\epsilon|^2 + \mu} \mathbf{Y}_c \right\} \quad (4)$$

We implement this reconstruction using the fast Fourier transform (FFT) and find that reconstructions take under one second to compute for 16-bit 4.2 megapixel images on a Dell Precision 5820 Workstation with a 14-core Intel Xeon W-2275 3.3 GHz CPU.

The eye's defocus error, and thus the corresponding  $\mathbf{h}_\epsilon$ , is unknown at the time of image capture. After image capture, a focal stack of reconstructed fundus images is created by deconvolving the

measurements,  $\mathbf{y}_\epsilon$ , with each PSF in the set of recorded  $\mathbf{h}_\epsilon$ . This is done for each color channel, producing a stack of color reconstructions for each  $\mathbf{x}_\epsilon$ . The focal stack can then be searched for the sharpest image manually or with an autofocus algorithm.

## 2.4. Calibration

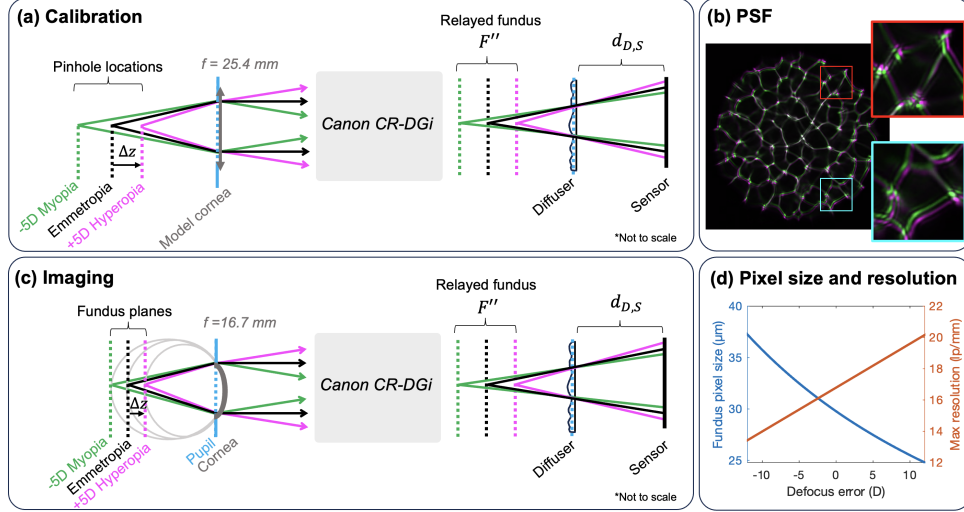


Fig. 3. Calibration overview. (a) The calibration of the system involves measuring PSFs of the system for a range of defocus errors,  $\epsilon$ . This is done by axially translating a 20-micron pinhole over a range of  $\Delta z$  from the backfocal plane of the model cornea. (b) Overlaid PSFs measured corresponding to -5D and +5D of defocus error (green and magenta, respectively), demonstrating the magnification difference. (c) An in vivo eye with a defocus error is modeled as having a fundus that is offset from the backfocal plane of the cornea by some  $\Delta z$ . The wavefront remitted from the pupil has a vergence dependent on the defocus error that is relayed to the diffuser. (d) The reconstruction pixel size and the corresponding maximum possible resolution as a function of defocus error.

The calibration of the system involves measuring a set of PSFs for points spanning a range of defocus errors. A motorized translation stage (LTS300, Thorlabs) was attached to a 20-micron diameter pinhole in front of a bright white LED (SLS-0300-C, Mightex). To simulate a point source on the retina of an emmetropic eye, the pinhole is placed a focal length behind a convex lens acting as a model cornea (LB1761-A,  $f=25.4 \text{ mm}$ , Thorlabs). The recorded signal on the image sensor is the PSF,  $\mathbf{h}_\epsilon$ , for the defocus error associated with the sampled  $\Delta z$ . We sampled PSFs from  $\Delta z = -12 \text{ mm}$  to  $\Delta z = +6 \text{ mm}$  with a sampling period of 50 microns, corresponding to defocus errors from -12D to +12D.

The PSF is dependent on defocus error,  $\epsilon$ , which can be computed from the focal length of the eye lens,  $f$ , and the distance of the object from the focus of the lens,  $\Delta z$ . The defocus error (in diopters) is simply the difference in optical powers:

$$\epsilon = \frac{1}{f_{\text{model}} - \Delta z} - \frac{1}{f_{\text{model}}} \quad (5)$$

By convention, defocus error associated with the object being too close to the lens (as is the case in hyperopia) is considered to be positive, and defocus error associated with the object being too far from the lens (as is the case in myopia) is considered to be negative.

## 2.5. Theoretical resolution and FOV

The magnification of the system can be computed with ray matrix analysis. We use a reduced eye model in this analysis, assuming that the eye is a thin lens with a power of 60 diopters,  $f_{\text{eye}} = 100/6$  mm. The distance between the cornea and fundus of an eye with a defocus error caused by an axial displacement of the fundus is  $f_{\text{eye}} - \Delta z$ . The system from the cornea to L3 is fixed and can be represented by a ray matrix,  $\begin{bmatrix} A & B \\ C & D \end{bmatrix}$ . The entire system matrix from the fundus,  $F$ , to the final conjugate fundus plane,  $F''$ , is represented by the matrix  $\mathbf{H}$ . The distance from L3 to the final conjugate fundus plane,  $F''$ , is  $d_{L3,F''}$  (see Fig. 2(c) for a diagram of the defined planes and Table 2 for a list of constants in the model). We can solve for the location of  $F''$  a function of  $\Delta z$  by applying the imaging condition to  $\mathbf{H}$ :

$$\mathbf{H} \begin{bmatrix} 0 \\ \theta_{\text{in}} \end{bmatrix} = \begin{bmatrix} 1 & d_{L3,F''} \\ 0 & 1 \end{bmatrix} \begin{bmatrix} A & B \\ C & D \end{bmatrix} \begin{bmatrix} 1 & f_{\text{eye}} - \Delta z \\ 0 & 1 \end{bmatrix} \begin{bmatrix} 0 \\ \theta_{\text{in}} \end{bmatrix} = \begin{bmatrix} 0 \\ \theta_{\text{out}} \end{bmatrix} \quad (6)$$

Solving (6) for  $d_{L3,F''}$ :

$$d_{L3,F''} = -\frac{A f_{\text{eye}} - A \Delta z + B}{C f_{\text{eye}} - C \Delta z + D} \quad (7)$$

Finally, the lateral magnification of the system from  $F$  to  $F''$ ,  $M_L$ , is the first element of the system matrix,  $H_{11}$ .

$$M_L = H_{11} = A + C d_{L3,F''} \quad (8)$$

The theoretical smallest resolvable feature of a lensless camera,  $R$  can be derived from the size of a sensor pixel,  $\delta$  mapped to the object plane [16].

$$R = \frac{d_{F'',D}}{d_{D,S}} * \frac{1}{M_L} * \delta \quad (9)$$

For our system,  $A = 0.921$ ,  $B = -35.4$ ,  $C = 0.0202$ ,  $D = 0.312$ , and  $\delta = 6.4$  microns. The distance from  $F''$  to the diffuser is  $d_{F'',D} = d_{L3,D} - d_{L3,F''}$ , where  $d_{L3,D}$  is the distance between L3 and the diffuser, which is equal to 111.6 mm in our system. Using these constants and combining equations (5), (7), (8), and (9) allows us to compute the pixel size and the associated Nyquist resolution limit in line pairs per millimeter in the fundus plane as a function of defocus error,  $\epsilon$  (Fig. 3(d)).

The Nyquist limit of the computational fundus camera is 18.9 lp/mm in an emmetropic eye with 60 diopters of power. This varies with defocus error due to a difference in magnification as described in (7)-(9) and ranges from 15 lp/mm in an eye with -12D myopia to 23 lp/mm in an eye with +12D hyperopia. This is a maximum possible resolution; in reality, noise and non-sparse objects will limit the resolution of the reconstructed measurements. This is within the Abbe diffraction limit of  $\approx 100 \text{ lp/mm}$  imaging the retina through the 1.4 mm diameter aperture stop.

The FOV of an image can be estimated with the pixel size on the fundus corresponding to the defocus error and focal length of the eye. The FOV of fundus cameras is typically reported in terms of visual angle, which is the full cone angle of light collected from the pupil of the eye. From the paraxial Zemax model, we estimate the FOV of this system to be 40 degrees.

## 2.6. In vivo imaging

Alignment is crucial for capturing high-quality in vivo fundus images. The illumination ring must align in the transverse plane to be concentric with the pupil, and the axial distance from the pupil to L1 must place the pupil conjugate to the diffuser. Alignment is performed by taking repetitive images with NIR illumination (740 nm, FWHM=30 nm) on undilated eyes in a dark

room to limit pupil constriction. The images are taken at 1-second intervals with an exposure of 40 ms, and reconstructions are shown live on a computer monitor. Once alignment is confirmed, three consecutive images with 40 ms exposures are taken using NIR (740 nm, FWHM=30 nm), green (550 nm, FWHM=60 nm), then blue (470 nm, FWHM=30 nm) illumination. The in vivo data was collected from healthy volunteers using an IRB-approved protocol (IRB 00333664). The light safety of the device was evaluated with ISO 15004-2. More detailed safety information is in Table 3 in the appendix.

### 3. Results

#### 3.1. Resolution target

To characterize the resolution of the system across a range of defocus errors, images of a USAF 1951 resolution target (R1DS1P, Thorlabs) were taken with the computational fundus camera and the conventional camera (Fig. 4). The resolution target was placed behind the model cornea at the focal distance. The captured image was deconvolved with (4) using regularization strength  $\mu = 0.001$ . The color channels were added together to eliminate differences in white balance between the separate images. To test the resolution on eyes with varying defocus errors, the resolution target was axially translated by hand and the image was computationally refocused. Translation distances were converted to defocus errors using (5). The translations,  $\Delta z$ , were kept under 6 mm, and 6 resolution test images were captured ranging from -3D to +12D of defocus error.

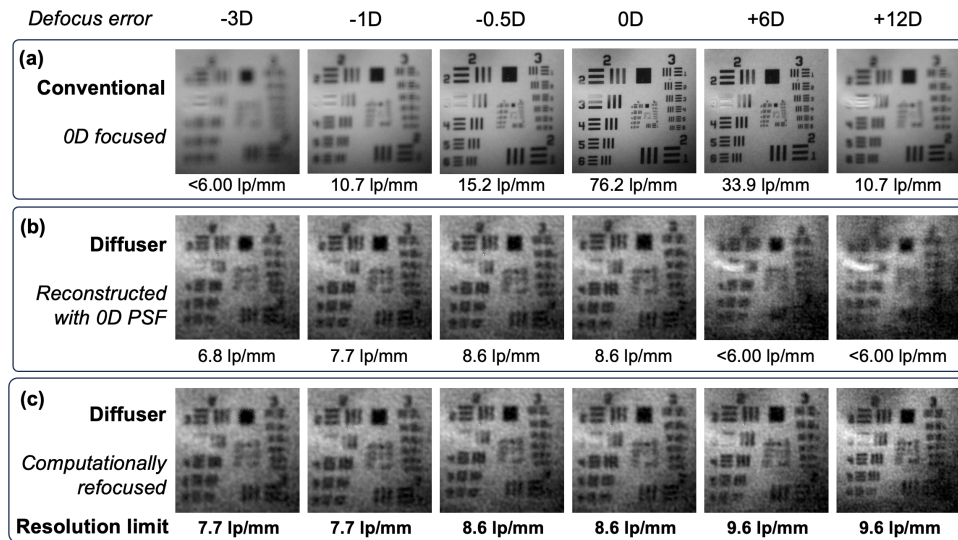


Fig. 4. Resolution evaluation of the system with a 1951 USAF resolution target. Defocus error was applied by adjusting the axial distance of the target behind a model cornea. The human eye-equivalent resolutions are shown, accounting for the difference in optical power between the human and model eye. (a) Cropped conventional camera images of the resolution target. The system was adjusted such that the target was in focus when positioned at 0D error. The resolution degrades sharply when the device is not focused. (b) Cropped diffuser images of the resolution target deconvolved with the 0D PSF. The resolution degrades with defocus error, but not as dramatically as the conventional camera. (c) The resolution of the diffuser images is improved compared to (b) when the correctly corresponding PSF is used to deconvolve the same measurement.

For comparison, conventional fundus photographs were taken with L2 fixed such that an object at 0D of error is in focus. Computational refocusing is done post-capture for the computational fundus camera with the optics remaining fixed. The resolution was estimated by examining the smallest set of line pairs that can be resolved. The mismatch between the power of the model eye cornea ( $f_{\text{model}} = 25.4$  mm) and the human eye ( $f_{\text{eye}} \approx 16.7$  mm) is accounted for with a magnification correction. After determining the resolution in lp/mm on the resolution target behind the model cornea, the result is multiplied by a factor of  $f_{\text{model}}/f_{\text{eye}} = 1.52$  to estimate the expected resolution in a human eye.

The resolution of the computational (diffuser-based) imaging system is 7.7-9.5 line pairs per mm (lp/mm) depending on the defocus error, as shown in Fig. 4. The resolution of the system increases with more hyperopic defocus due to the increased magnification of the fundus, as expected (Fig. 3(d)). The resolution is still poorer than the conventional lens-based image, which has a peak of 76.2 lp/mm for an emmetropic (0D) eye when the system has the focus set to 0D. However, this resolution quickly falls off for the conventional lens-based camera with defocus error applied. Meanwhile, the resolution of the refocused computational image remains in the 7.7-9.5 lp/mm range for all tested defocus errors (from -3D to +12D).

### 3.2. Model eye

Next, we tested our system on a commercial model eye (Ophthalmoscope Trainer, HEINE), which has an adjustable length to simulate defocus errors from -5D to +5D of defocus error. Diffuser images of the model eye were taken with the model eye adjusted to be -5D myopic, 0D emmetropic, and +5D hyperopic. For comparison, conventional fundus photographs were taken with the camera lenses adjusted and fixed such that an object at 0D of error is in focus.

The results in Fig. 5 show the reconstructions of the model eye with a visible optic disk and fovea. The reconstructions were computed with (4) using  $\mu = 0.002$  for each color channel. The conventional image and diffuser image have a similar FOV, which is approximately the  $40^\circ$  FOV inherent to the optical design of the Canon CR-DGi. The FOV was estimated using the theoretical pixel size computed with (9). Refocusing to the proper defocus error results in the sharpest reconstruction. The resolution of the sharpest diffuser-based reconstruction is worse than the resolution of the focused conventional image. However, the computational images in Fig. 5(b) can be computationally refocused post-capture, while a high-quality conventional image requires precise adjustment prior to image capture.

### 3.3. In vivo images

We present the first diffuser-based computational images of an in vivo fundus (Fig. 6). Computational refocusing enables images to be optimally resolved without prior knowledge of the patient's refractive error, and no adjustments are made to the optical system during or prior to capture to compensate. The macula, optic disk, choroidal structure, and vessels are visible in the refocused reconstruction. The red, green, and blue color channels are created from three consecutively captured images with 40 ms exposures each and overlaid. The regularization strength was tuned separately for each color channel and was chosen to be  $\mu = 0.007$  for red,  $\mu = 0.002$  for green, and  $\mu = 0.02$  for blue. The green channel contains the most contrast due to the absorption of green light by blood vessels. The blue channel contains the least contrast. More information on the selection of regularization strength is in appendix section 4.3.

## 4. Discussion

### 4.1. Resolution

The resolution of the diffuser-based system was shown to be  $\sim 7$ -10 lp/mm across a range of defocus errors (Fig. 4). This is less than the maximum theoretical resolution of 13-20 lp/mm

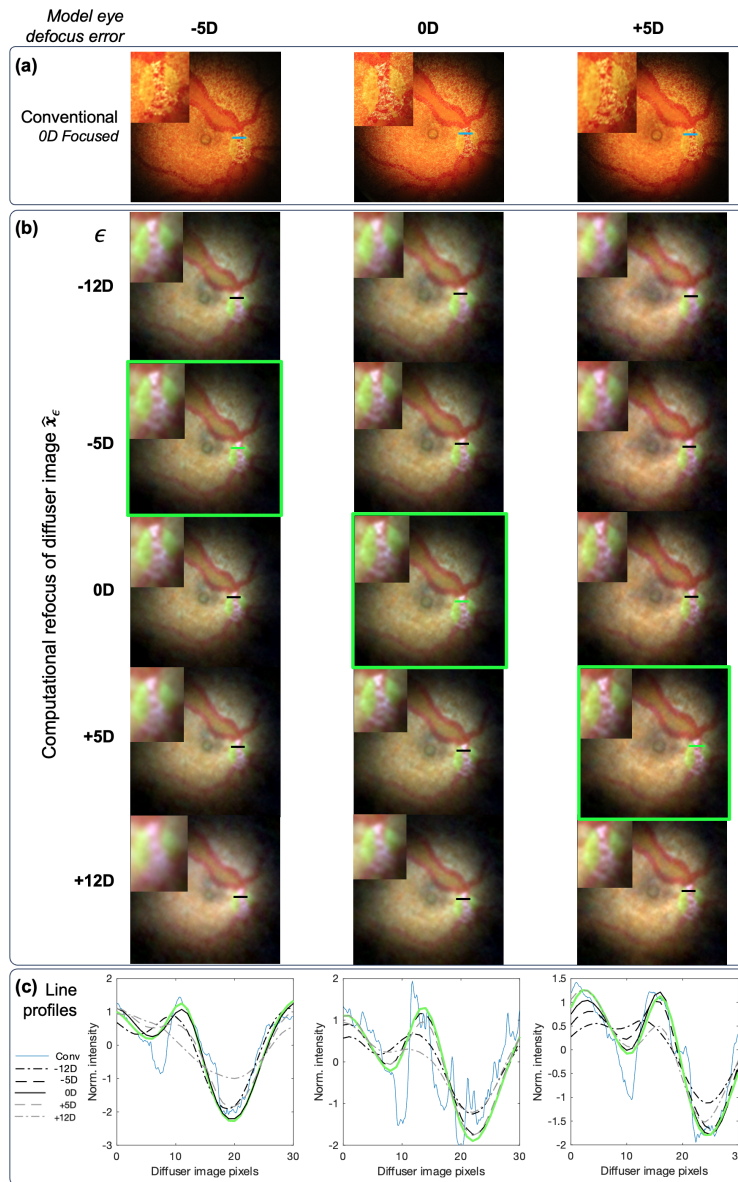


Fig. 5. Demonstration of computational refocusing in the HEINE model eye measured with defocus errors of -5D (first column), 0D (second column), and +5D (third column). (a) Conventional camera images with focus set to 0D. (b) Computationally refocused diffuser images using different PSFs. The diagonal indicated by green boxes contains the sharpest images when deconvolving with the corresponding PSF. The reconstructions are blurrier when the difference between the defocus error of the eye and the  $\epsilon$  used for  $h_\epsilon$  is greater. (c) Line profiles through the optic disk for each row. Among diffuser images, the contrast is the greatest in the correctly refocused image (green line for each row). The line profiles are normalized with the same multiplicative factor and centered to the mean. Images (a, i, p) are corresponding conventional camera images with the camera set to image an emmetropic eye.

(Fig. 3(d)). This is partly attributable to our scenes being very dense, making the inverse problem poorly conditioned [24], even though we used a low-noise, 16-bit sensor. In general, the resolution of phase-mask based imaging systems is dependent on the sparsity of the object. The resolution of the diffuser-based computational fundus camera is poorer than a properly focused conventional camera, consistently evidenced by the imaging of the resolution target (Fig. 4), the model eye (Fig. 5), and the in vivo eye (Fig. 6). However, the computational image performs nearly identically across eyes with a very wide range of defocus errors with no prior adjustment, while the conventional camera requires precise focusing to maximize its resolution.

#### 4.2. In vivo imaging

The results demonstrate that the diffuser-based computational fundus camera allows single-shot imaging of the fundus with no focusing required before image capture and can reconstruct images of the fundus over a large range of defocus errors. The in vivo FOV is approximately 40 degrees, which was estimated using the theoretical pixel size for a 60 diopter eye with -8.6 diopters of myopia. This FOV is common for non-mydratic fundus cameras used for screening. Important clinical features, including the optic disk, macula, and larger blood vessels are resolved in both

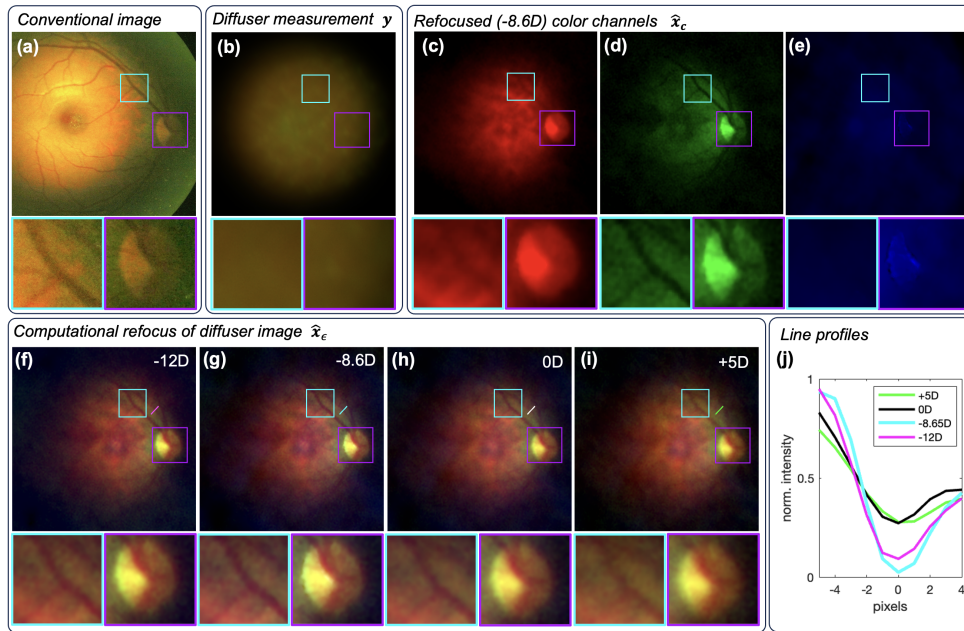


Fig. 6. (a) Conventional camera image of an in vivo fundus. (b) Raw diffuser camera measurement of the fundus with RGB images combined. (c-e) Reconstructions of the individual red, green, and blue illumination measurements, computationally refocused to -8.6 diopters, which was manually selected from the focus stack. The green channel (d) provides the most vessel and optic disk contrast. (f-i) Computational refocusing of the combined RGB fundus image. The optic disk, blood vessels, and choroidal structure are observed. (g) The sharpest image corresponds to -8.6 diopters. (j) Line profiles of the green channel across the same vessel in (f-i). The -8.6D reconstruction has the greatest contrast and sharpest vessel boundaries while refocusing to other levels reduces vessel contrast and results in smoother edges. Cyan and Purple box insets for each large field of view image are magnified and displayed below for better comparison of vessel and optical disk contrast.

the model eye and in vivo human eye. Computational refocusing increased the visibility and contrast of the blood vessels (Figure 6).

There are several limitations of our in vivo fundus imaging approach. We did not have a fixation target, which made alignment and control of instrument-induced myopia difficult. Non-mydratric fundus imaging presents further challenges by having a smaller pupil to image through, and any exposure to bright visible light causes the pupil to dramatically constrict, blocking illumination with the iris. Therefore, alignment must be achieved with low-contrast deep red/NIR illumination, and the visible light image must be taken with an exposure faster than the pupillary light reflex. Finally, the resolution is worse than a clinical fundus camera (which typically have resolutions greater than 50 lp/mm). Future work will require increasing the resolution to ensure the diagnostic capabilities of the system.

### 4.3. Deconvolution methods

Our deconvolution method is the same as Li et al. [20] and is computationally simple. The Tikhonov inverse problem has a closed-form solution (regularized inverse filter) with no iteration required, making the reconstruction of a single image take approximately 200 ms and a focal stack of 500 images take less than 2 minutes. However, there is room for improvement with the use of more sophisticated priors. The regularization factor in (3) is the  $L_2$ -norm of the object. This penalizes large values in the reconstruction, which in effect reduces the variance, smoothing the image. However, there are regularization factors that better balance the prior knowledge of the features of natural images while maintaining a stable reconstruction. For example, the regularization factor could be made to be the  $L_2$ -norm of the gradient of the object, which limits the power of the gradient, or the  $L_1$ -norm of the gradient of the object (also called total variation), which enforces sparsity in the gradient. These are more powerful assumptions for fundus images, which are mostly bright and flat, with thin, dark features. However, these regularizers significantly increase computational complexity because the solution must be solved iteratively. Other options are deep-learning models that may better reconstruct images while taking into account the spatial variance of the PSF [25].

The regularization strength,  $\mu$ , used for our reconstructions in Fig. 6 was chosen manually. After creating the focal stack using  $\mu = 0.007$  as a standard regularization strength, a stack of reconstructions using the correct PSF and a range of  $\mu$  from 0.001 to 0.025 was created for each color channel. Then, the image that subjectively balances sharpness with noise in each color channel was chosen. For red, this was chosen to be  $\mu = 0.007$ , green used  $\mu = 0.002$ , and blue used  $\mu = 0.02$ . The use of different  $\mu$  for the different channels can be justified by examining the generalization of the regularized inverse filter, (4), which is the Wiener filter [26].

$$\hat{\mathbf{x}}_{\epsilon,c} = \mathcal{F}^{-1}\{\hat{\mathbf{X}}_{\epsilon,c}\} = \mathcal{F}^{-1}\left\{\frac{\mathbf{H}_{\epsilon}^*}{|\mathbf{H}_{\epsilon}|^2 + \frac{1}{SNR(u,v)}}\mathbf{Y}_c\right\} \quad (10)$$

Where  $SNR(u, v)$  is the ratio of the power spectrum of the underlying image  $x$  to the noise power spectrum. This means that the optimal solution in minimum mean square error sense with knowledge of noise power spectra and the power spectrum of the underlying image is a regularized inverse filter with a  $\mu$  dependent on the signal-to-noise ratio (SNR) of each frequency component. In other words, (4) can be regarded as a Wiener filter with the assumption of a flat SNR across all frequencies. This form of the Wiener filter is difficult to utilize because the underlying power spectrum of the object is not generally known. However, it is known that the green channel has a higher SNR for a greater bandwidth of spatial frequency due to stronger high-frequency content arising from high-contrast blood vessels. This means that a lower  $\mu$  for the green channel would approximate the regularized inverse filter closer to an ideal Wiener filter. Likewise, the lower SNR across a smaller bandwidth of frequencies for the lower signal blue channel would demand a higher  $\mu$  to better approximate the Wiener filter.

#### 4.4. Future work

Deconvolution of dense objects like the fundus is difficult with a phase mask that produces an extended PSF [24]. Future work using phase-mask elements with sparser PSFs, such as random microlens arrays, could improve the resolution of the system [27]. Other groups have found that random microlens arrays have better resolution than holographic diffusers for computational imaging [28], while the randomness alleviates the aliasing concerns associated with periodic microlens arrays. A specially designed phase mask for the computational fundus camera should balance the requirements of resolution and computational refocusing over the range of clinically relevant refractive errors. Specialized phase masks could also be designed to efficiently multiplex aberrometry information, including spherical and cylindrical errors, into the measurement. McKay et al. have already explored diffuser-based aberrometry, which uses a similar configuration to this system [29].

Commercial low-cost handheld autorefractors have been developed that promise to expand access to eyeglass prescriptions [30, 31]. We believe that phase mask-based fundus imaging could be leveraged to create a similar device that simplifies image capture and combines fundus imaging and autorefraction into a single measurement with a simple optical system. This would have great potential to reduce costs, increase throughput, and deskill the comprehensive eye examination. This could allow for single-shot aberrometry and fundus photography with no prior focusing required. Future reconstruction methods could involve synergistically reconstructing while performing wavefront sensing to improve the quality of the image and provide eyeglass prescriptions.

## 5. Conclusion

Access to eye diagnostic care could be improved with easier-to-use, higher-throughput diagnostic tools. This work builds upon the work of Antipa et al. [15] and Li et al. [20] to create a diffuser-based fundus camera that enables post-capture computational refocusing of the fundus, circumventing one of the challenging steps in obtaining a high-quality fundus image. We demonstrate computational refocusing in vivo fundus images across a wide range of clinically relevant defocus errors. The resolution computational of the system is consistent across many diopters of defocus error without the need for moving parts. The FOV is comparable to that of a standard non-mydratic fundus camera. However, the resolution is less than a conventional fundus camera, limited by the smoothness and spread of the diffuser PSF. This limitation can be addressed with better encoding elements, such as random microlens arrays. Lastly, there is an opportunity for future work that synergistically estimates aberrometry information and reconstructs a fundus image from a single measurement.

## 6. Appendix

### 6.1. System setup

Placement of the diffuser conjugate to the pupil is necessary for the PSF of the system to be shift-invariant. This is verified by translating the pinhole transversely behind the model cornea while observing the PSF created on the image sensor. The axial location of the diffuser was then fine-tuned with a translation stage until the PSF was maximally shift-invariant. During our testing, we also found that the diffuser-sensor distance ( $d_c$ ) was important to optimize for the sharpest caustic pattern to form. This reduces the spread of the PSF which improves the conditioning of the inverse problem. We achieved this by placing the pinhole behind the model cornea at an emmetropic distance and translating the camera axially while observing the sharpness of the caustic pattern formed on the image sensor.

The Zemax model shown in Figs. 2 and 7 was made using only paraxial (thin) lenses. The lenses that are part of the Canon CR-DGi (L1, L2, L4, and L5) do not have publicly accessible

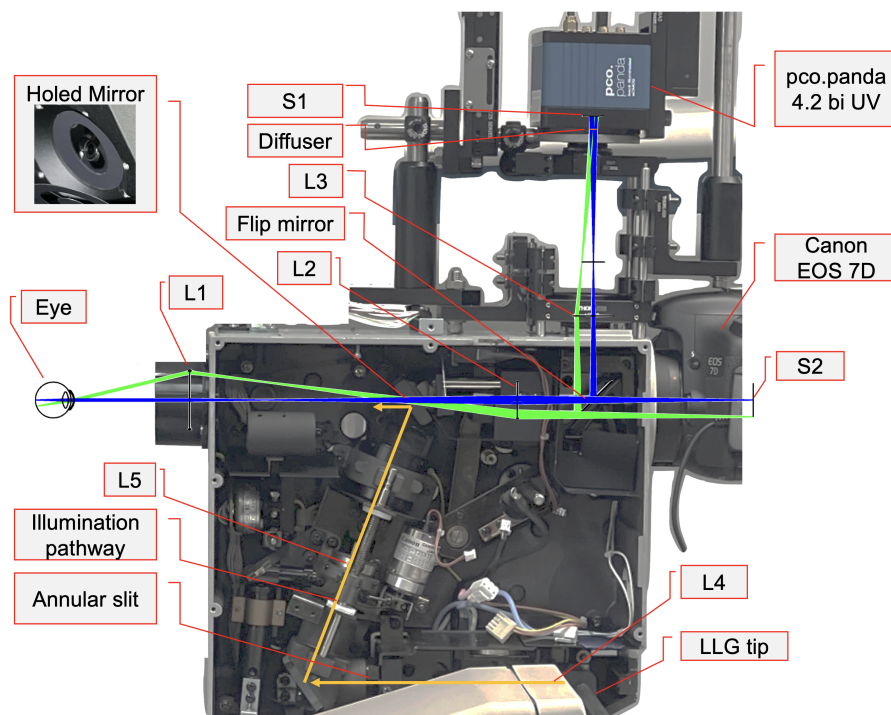


Fig. 7. Photograph of the system with labeled components. The diffuser camera is connected to the top of the commercial fundus camera, replacing the conventional IR alignment camera. The internal electrical components of the fundus camera were removed, and the inside of the Canon CR-DGi fundus camera was used for its optics. Zemax models of the diffuser imaging and conventional imaging path are overlaid. The entire system is mounted to a translating base that eases the alignment process. An ophthalmic chinrest is used to stabilize the patient's head (not pictured).

parameters. The focal lengths for these components were estimated using the thin lens equation and measured distances between the conjugate planes of the system. The parameters of the Zemax model are in Table 2.

## 6.2. Light safety

The device was evaluated for light safety according to ISO 15004-2009, which specifies light hazard protection for ophthalmic devices. This protocol specifies the maximum irradiance on the cornea and fundus, considering the thermal hazard, aphakic photochemical hazard, and ultraviolet hazard. For each wavelength band used, the device was determined to be Group 1, indicating that it is non-hazardous for human use. The maximum irradiances for the different wavelengths are shown in the Table 3. In practice, the power used for each color band was restricted to less than these values.

Table 1. Optical components in the computational imaging pathway.

Part name	Description	Part no.	Manufacturer	Focal length (mm)	Diameter (mm)
L1	Objective		Canon	42*	50.8
L2	Relay		Canon	75*	25.4
L3	Diffuser relay	AC254-100-A	Thorlabs	100	25.4
D	Diffuser	#47-988	Edmund Optics	$\approx 11^*$	25.4
C	Model cornea	LB1761-A	Thorlabs	25.4	25.4
C	Model eye	C-000.33.010	HEINE	18	8
C	In vivo eye			100/6	8

\* represents a computed or estimated value

Table 2. List of variables in system model.

Variable	Description	Value
$f_{eye}^*$	In vivo eye	100/6 mm
$f_{HEINE}$	HEINE model eye	18 mm
$f_{model}$	Model cornea	25.4 mm
$d_{P,L1}$	Pupil to L1 dist.	70.85 mm
$f_{L1}^*$	Objective lens	46.2 mm
$d_{L1,HM}$	L1 to HM dist.	132.8 mm
$d_{HM,L2}$	HM to L2 dist.	68.75 mm
$f_{L2}^*$	Relay lens	75 mm
$d_{L2,L3}$	L2 to L3 dist.	96.75 mm
$f_{L3}$	Diffuser relay lens	100 mm
$d_{L3,D}$	L3 to D dist.	111.6 mm
$d_{D,S}$	Diffuser sensor dist.	11.0 mm

\* represents a computed or estimated value

**Funding.** This work is supported by the Wilmer Eye Institute Pooled Professor Fund and the unrestricted grant from Research to Prevent Blindness (RPB).

**Disclosures.** NJD is listed as co-inventor on a provisional patent application assigned to Johns Hopkins University that is related to the technologies described in this article. They may be entitled to future royalties from this intellectual property.

Table 3. Summary of the maximum irradiances for the wavelengths used by the computational fundus camera.

Wavelength (nm)	Total power output (mW)	Anterior segment irradiance (mW/cm <sup>2</sup> )	Fundus irradiance (mW/cm <sup>2</sup> )	Passes all ISO limits for Group 1
470 (blue)	5.90	74	7.4	Yes
550 (green)	5.66	71	7.1	Yes
740 (red)	3.60	45	4.5	Yes

**Data Availability Statement.** Data may be obtained from the authors upon reasonable request.

## References

1. Q. V. Hoang, "Adult Eye Examination Techniques," in *The Columbia Guide to Basic Elements of Eye Care: A Manual for Healthcare Professionals*, D. S. Casper and G. A. Cioffi, eds. (Springer International Publishing, Cham, 2019), pp. 27–36.
2. S. R. Flaxman, R. R. A. Bourne, S. Resnikoff, *et al.*, "Global causes of blindness and distance vision impairment 1990–2020: a systematic review and meta-analysis," *The Lancet Glob. Health* **5**, e1221–e1234 (2017). Publisher: Elsevier.
3. P. Bragge, R. L. Gruen, M. Chau, *et al.*, "Screening for Presence or Absence of Diabetic Retinopathy: A Meta-analysis," *Arch. Ophthalmol.* **129**, 435–444 (2011).
4. E. K. Chin, B. V. Ventura, K.-Y. See, *et al.*, "Nonmydriatic Fundus Photography for Teleophthalmology Diabetic Retinopathy Screening in Rural and Urban Clinics," *Telemedicine e-Health* **20**, 102–108 (2014). Publisher: Mary Ann Liebert, Inc., publishers.
5. C. Bascaran, N. Mwangi, F. D'Esposito, *et al.*, "Effectiveness of task-shifting for the detection of diabetic retinopathy in low- and middle-income countries: a rapid review protocol," *Syst. Rev.* **10**, 4 (2021).
6. R. Bernardes, P. Serranho, and C. Lobo, "Digital Ocular Fundus Imaging: A Review," *Ophthalmologica* **226**, 161–181 (2011).
7. E. DeHoog and J. Schwiegerling, "Optimal parameters for retinal illumination and imaging in fundus cameras," *Appl. Opt.* **47**, 6769–6777 (2008). Publisher: Optica Publishing Group.
8. O. Bergamin and R. H. Kardon, "Latency of the Pupil Light Reflex: Sample Rate, Stimulus Intensity, and Variation in Normal Subjects," *Investig. Ophthalmol. & Vis. Sci.* **44**, 1546–1554 (2003).
9. N. Panwar, P. Huang, J. Lee, *et al.*, "Fundus Photography in the 21st Century—A Review of Recent Technological Advances and Their Implications for Worldwide Healthcare," *Telemedicine J. e-Health* **22**, 198–208 (2016).
10. N. J. Durr, S. R. Dave, E. Lage, *et al.*, "From Unseen to Seen: Tackling the Global Burden of Uncorrected Refractive Errors," *Annu. Rev. Biomed. Eng.* **16**, 131–153 (2014). Publisher: Annual Reviews.
11. X. Yao, T. Son, and J. Ma, "Developing portable widefield fundus camera for teleophthalmology: Technical challenges and potential solutions," *Exp. Biol. Med.* **247**, 289–299 (2022). Publisher: SAGE Publications.
12. N. M. Bolster, M. E. Giardini, and A. Bastawrous, "The Diabetic Retinopathy Screening Workflow: Potential for Smartphone Imaging," *J. Diabetes Sci. Technol.* **10**, 318–324 (2016). Publisher: SAGE Publications Inc.
13. T. W. Rogers, J. Gonzalez-Bueno, R. Garcia Franco, *et al.*, "Evaluation of an AI system for the detection of diabetic retinopathy from images captured with a handheld portable fundus camera: the MAILOR AI study," *Eye* **35**, 632–638 (2021). Publisher: Nature Publishing Group.
14. B. L. Shou, K. Venkatesh, C. Chen, *et al.*, "Predictors for Non-Diagnostic Images in Real World Deployment of Artificial Intelligence Assisted Diabetic Retinopathy Screening," *Investig. Ophthalmol. & Vis. Sci.* **63**, 1157 (2022).
15. N. Antipa, G. Kuo, R. Heckel, *et al.*, "DiffuserCam: lensless single-exposure 3D imaging," *Optica* **5**, 1–9 (2018). Publisher: Optica Publishing Group.
16. V. Boominathan, J. K. Adams, J. T. Robinson, and A. Veeraghavan, "PhlatCam: Designed Phase-Mask Based Thin Lensless Camera," *IEEE Trans. on Pattern Anal. Mach. Intell.* **42**, 1618–1629 (2020). Conference Name: IEEE Transactions on Pattern Analysis and Machine Intelligence.
17. N. Antipa, S. Necula, R. Ng, and L. Waller, "Single-shot diffuser-encoded light field imaging," in *2016 IEEE International Conference on Computational Photography (ICCP)*, (2016), pp. 1–11.
18. Z. Cai, J. Chen, G. Pedrini, *et al.*, "Lensless light-field imaging through diffuser encoding," *Light. Sci. & Appl.* **9**, 143 (2020). Number: 1 Publisher: Nature Publishing Group.

19. V. Boominathan, J. T. Robinson, L. Waller, and A. Veeraraghavan, "Recent advances in lensless imaging," *Optica* **9**, 1–16 (2022). Publisher: Optica Publishing Group.
20. Y. Li, G. N. McKay, N. J. Durr, and L. Tian, "Diffuser-based computational imaging funduscope," *Opt. Express* **28**, 19641–19654 (2020). Publisher: Optica Publishing Group.
21. T. T. J. M. Berendschot, P. J. DeLint, and D. v. Norren, "Fundus reflectance—historical and present ideas," *Prog. Retin. Eye Res.* **22**, 171–200 (2003).
22. E. DeHoog and J. Schwiegerling, "Fundus camera systems: a comparative analysis," *Appl. optics* **48**, 221–228 (2009).
23. A. Murli, L. D'Amore, and V. De Simone, "The Wiener filter and regularization methods for image restoration problems," in *Proceedings 10th International Conference on Image Analysis and Processing*, (1999), pp. 394–399.
24. J. K. Adams, D. Yan, J. Wu, *et al.*, "In vivo lensless microscopy via a phase mask generating diffraction patterns with high-contrast contours," *Nat. Biomed. Eng.* **6**, 617–628 (2022). Number: 5 Publisher: Nature Publishing Group.
25. K. Yanny, K. Monakhova, R. W. Shuai, and L. Waller, "Deep learning for fast spatially varying deconvolution," *Optica* **9**, 96–99 (2022). Publisher: Optica Publishing Group.
26. R. C. Gonzalez and R. E. Woods, *Digital image processing* (Pearson, New York, NY, 2018), fourth edition, global edition ed.
27. F. L. Liu, G. Kuo, N. Antipa, *et al.*, "Fourier DiffuserScope: single-shot 3D Fourier light field microscopy with a diffuser," *Opt. Express* **28**, 28969–28986 (2020). Publisher: Optica Publishing Group.
28. G. Kuo, F. L. Liu, I. Grossrubatscher, *et al.*, "On-chip fluorescence microscopy with a random microlens diffuser," *Opt. Express* **28**, 8384–8399 (2020). Publisher: Optica Publishing Group.
29. G. N. McKay, F. Mahmood, and N. J. Durr, "Large dynamic range autorefraction with a low-cost diffuser wavefront sensor," *Biomed. Opt. Express* **10**, 1718–1735 (2019). Publisher: Optica Publishing Group.
30. N. J. Durr, S. R. Dave, F. A. Vera-Diaz, *et al.*, "Design and Clinical Evaluation of a Handheld Wavefront Autorefractor," *Optom. Vis. Sci.* **92**, 1140 (2015).
31. N. J. Durr, S. R. Dave, D. Lim, *et al.*, "Quality of eyeglass prescriptions from a low-cost wavefront autorefractor evaluated in rural India: results of a 708-participant field study," *BMJ Open Ophthalmol.* **4**, e000225 (2019). Publisher: BMJ Specialist Journals Section: Original article.